PIV–LES analysis of channel flow rotating about the streamwise axis

I. Recktenwald[*], N. Alkishriwi, W. Schröder

Chair of Fluid Mechanics and Institute of Aerodynamics, RWTH Aachen University, Wüllnerstraße 5a, D-52062 Aachen, Germany

ARTICLE INFO

ABSTRACT

The flow field of a channel rotating about the streamwise axis is analyzed experimentally and numerically. The current investigations were carried out at a bulk velocity based Reynolds number of $Re_m = 2850$ and a friction velocity based Reynolds number of $Re_\tau = 180$, respectively. Particle-image velocimetry (PIV) measurements are compared with large-eddy simulation data to show earlier direct numerical simulation findings to generate too large a reverse flow region in the center region of the spanwise flow. The development of the mean spanwise velocity distribution and the influence of the rotation on the turbulent properties, i.e., the Reynolds stresses and the two-point correlations of the flow, are confirmed in both investigations. The rotation primarily influences those components of the Reynolds shear stresses, which contain the spanwise velocity component. The size of the correlation areas and thus the length scales of the flow generally grow in all three coordinate directions leading to longer structures. Furthermore, experimental results of the same channel flow at a significantly lower bulk Reynolds number of $Re_{m,\, l} = 665$, i.e., a laminar flow in a non-rotating channel, are introduced. The experiments show the low Reynolds number flow to become turbulent under rotation and to develop the same characteristics as the high Reynolds number flow.

1. Introduction

Rotating flows, such as rotating channel flows, are of major interest today, especially in computational fluid dynamics (CFD). This is due to the fact that particularly Reynolds-averaged Navier–Stokes (RANS) solvers using two-equation models, which are extremely often used to simulate turbulent flows, have problems to resolve the effects that arise in rotating fluids. As a matter of fact, even higher-order turbulence models do, though to a lower extent.

Although rotating channel flows have been investigated experimentally and numerically by, e.g., Hart [1], Johnston et al. [2], Kristoffersen and Andersson [3], or Tafti and Vanka [4], the rotation about the streamwise axis has experienced some analysis only recently. First investigations showed the development of a secondary flow profile perpendicular to the main flow and a deviation of the main flow, which could not at all be obtained when a second-moment closure model was used. Only higher-order models such as Reynolds stress transport models and large-

eddy simulations (LES) were able to at least qualitatively determine the induced secondary flow and the influence on the main flow [5]. These flow deviations also have been observed by Wu and Kasagi [6] who simulated rotation about the streamwise axis as a limit case of non-orthogonal, i.e., arbitrary system rotation.

Even though some numerical research has been done recently, an experimental investigation of flow rotating about the streamwise axis has been done only recently [7]. As was found in comparing numerical and experimental data, especially the DNS results showed a distinct difference to the experimental results, i.e., they contained a pronounced reverse flow region near the channel center, such that the induced flow possesses the structure of two counter-rotating swirls. The experimental results do not show this behavior, the secondary flow is limited to a distinct development of a velocity near the wall. A weak reverse flow occurs only at very high rotation rates [7]. That is, especially at low rotation rates the recirculation structure near the axis cannot be confirmed at all by the measurements. This clear discrepancy was weakened by a recent large-eddy simulation which shows a much better agreement with the experimental findings than the currently available DNS results [8]. To be more precise, the LES evidenced a much smaller reverse velocity near the axis than the DNS. Although the LES findings do not perfectly match the measurements the much closer agreement with the experimental distributions initiated further analyses to substantiate the flow structure which is unlike

* Corresponding author.
E-mail addresses: i.recktenwald@aia.rwth-aachen.de (I. Recktenwald), n.alkishriwi @aia.rwth-aachen.de (N. Alkishriwi), office@aia.rwth-aachen.de (W. Schröder).
URL: http://www.aia.rwth-aachen.de

the DNS data from the literature characterized by a spanwise velocity distribution being dominated by a pronounced peak near the wall. That is, the spanwise velocity near the axis is insignificant compared to its strength near the walls.

In other words, the purpose of this study is to compare in detail LES and experimental data on one hand, to shed some light on the discrepancy between the DNS and experimental data and on the other hand, to evidence the characteristic flow features. To be more precise, it was conjectured, for instance, in [7] that the spanwise extent of the computational domain does not impact the mean flow structure. This statement will be discussed in detail in this article. That is, the spanwise extension of the computational domain and as such the use of periodic or no-slip boundary conditions, will be shown to hardly influence the fundamental flow pattern if the spanwise extent is larger than a certain limit.

The LES findings indicate the DNS data to differ from the experimental secondary flow in [7] possibly due to too small a spanwise extension of the domain. That is, the use of an integration domain in the spanwise direction similar to that used by Kim et al. [9] for the non-rotating case is inappropriate for the rotating channel flow. This domain has to be increased significantly especially in the spanwise direction to correctly capture the effects generated by the Coriolis forces which are observed in the experiments. In completing the analyses presented in [7,8] this issue is discussed at length in this study.

Furthermore, the comparison of the turbulent properties, i.e., the distributions of the root mean square values and two-point correlations, of the LES solution and the PIV measurements is given to point out that the fluctuations in the streamwise direction are affected less than it was proposed based on the DNS results. To complete the survey of the influence of axial rotation on channel flow, the results of experiments at a lower Reynolds number, i.e., $Re_{m,l} = 665$ are presented. They evidence the destabilizing effect of axial rotation on laminar channel flow. These measurements also show, that the revolution history of the flow has no qualitative impact on the spanwise velocity distribution.

The flow parameters were required to match the well-documented non-rotating channel flow by Kim et al. [9] and the experiments and the numerical simulations were performed under flow conditions as similar as possible. Especially, when simulating the influence of the spanwise walls a computational domain with a span width of $20\,h$ was used, with h being the channel half-height, analogous to the smallest channel span width realized in the experiments. Thus, the results could be directly compared.

Besides this Introduction the paper contains three additional sections. In Section 2 the experimental setup and the numerical method will be briefly explained. In Section 3 the experimental and numerical results of several rotation rates and the non-rotating channel flow are juxtaposed and analyzed. Also, the experimental results of rotating flow at $Re_{m,l} = 665$, i.e., at a Reynolds number ensuring a laminar flow at a non-rotating channel, are presented and discussed. Finally, the essential findings will be summarized.

2. Experimental setup and numerical method

To allow a basic understanding of the experimental and numerical setup, a short outline of the measurement and computational methods and the parameters, especially those differing from previous publications, are given. Further details on the channel setup, the measuring system, and the image data processing are presented in [7]. A more thorough description of the numerical method and the details of the computational domain and the boundary conditions can be found in [8].

2.1. Channel setup

The measurements were done in a rotating channel with a length $L = 2$ m, a width $W = 0.2$ m, and a height $H = 0.02$ m. The span width of $W = 0.2$ m $= 10H$ agrees exactly with the size of the computational domain used in the LES. Note, to investigate the impact of the spanwise extent the channel width could be altered to $W = 0.5$ m and $W = 1.0$ m. A sketch of the channel and the details of the complete setup are shown in Fig. 1. The definition of the coordinate system is given in Fig. 2. The Reynolds number $Re_m = Uh/\nu = 2850$ is determined using the mean bulk velocity

$$U = \frac{1}{T}\frac{1}{A}\iint\limits_{T\,A} u(y,z,t)\,\mathrm{d}A\mathrm{d}t \tag{1}$$

and the channel half-height $h = H/2$. The geometry and flow data of the channel setup are summarized in Table 1. An overview of the flow variations and the corresponding characteristics can be found in Table 3.

2.2. PIV-system

The particle-image velocimetry (PIV) technique was used to perform the measurements. The stereo system consisted of two PCO SensiCam CCD double-shutter cameras with a resolution of 1280×1024 pixel in conjunction with double telecentric lenses, which were set up to satisfy the Scheimpflug condition such that the pictures remained orthogonal [10]. Details of the camera setup are shown in Fig. 3.

The plate, which the whole setup was mounted on, could be rotated about the laser sheet axis, such that the light sheet could be aligned either in the streamwise or the spanwise direction (Fig. 4). The pulse distance at $Re_m = 2850$ corresponded to 500 µs for the streamwise oriented light sheet and to 250 µs for the spanwise orientation, respectively. The pulse distance was changed for the measurements at $Re_{m,l} = 665$. Here, the corresponding values were set to 1000 µs for the streamwise and 750 µs for the spanwise orientation. A summary of the parameters of the PIV-system is given in Table 2.

2.3. Large-eddy simulation

The large-eddy simulations have been performed on a computational domain at $L = W = 20\,h$ in the streamwise x- and spanwise z-direction and $H = 2h$ in the wall-normal y-direction, where $h = H/2$ is the channel half-height. The Reynolds number $Re_\tau = 180$ was based on the friction velocity u_τ and the Rossby numbers $Ro_m = U/(fh) = \infty$, $Ro_m = 65.2$, and $Ro_m = 37.5$ were defined by the mean bulk velocity U. The mesh contains 6,114,083 cells, 153 of which are distributed in the x-direction, 89 in the y-direction, and 449 in the z-direction. The minimum space step in the normal direction is $\Delta y+ = 1$ in inner wall units. To ensure the highest possible degree of analogy between the computations and the experiments, periodicity is prescribed in the x-direction and the no-slip condition is imposed on the walls in the y- and z-direction, generating an actual channel flow with the same geometry as in the experiment.

The scheme is described in detail and validated against several test problems such as channel, jet, and pipe flows in [11] and [12]. The method is formulated for multiblock structured curvilinear grids and implemented on vector and parallel computers. To enable an efficient analysis even in the low Mach number regime a preconditioned LES method has been developed [13].

To validate the method of solution and to identify the changes due to rotation, a non-rotating channel flow also was simulated.
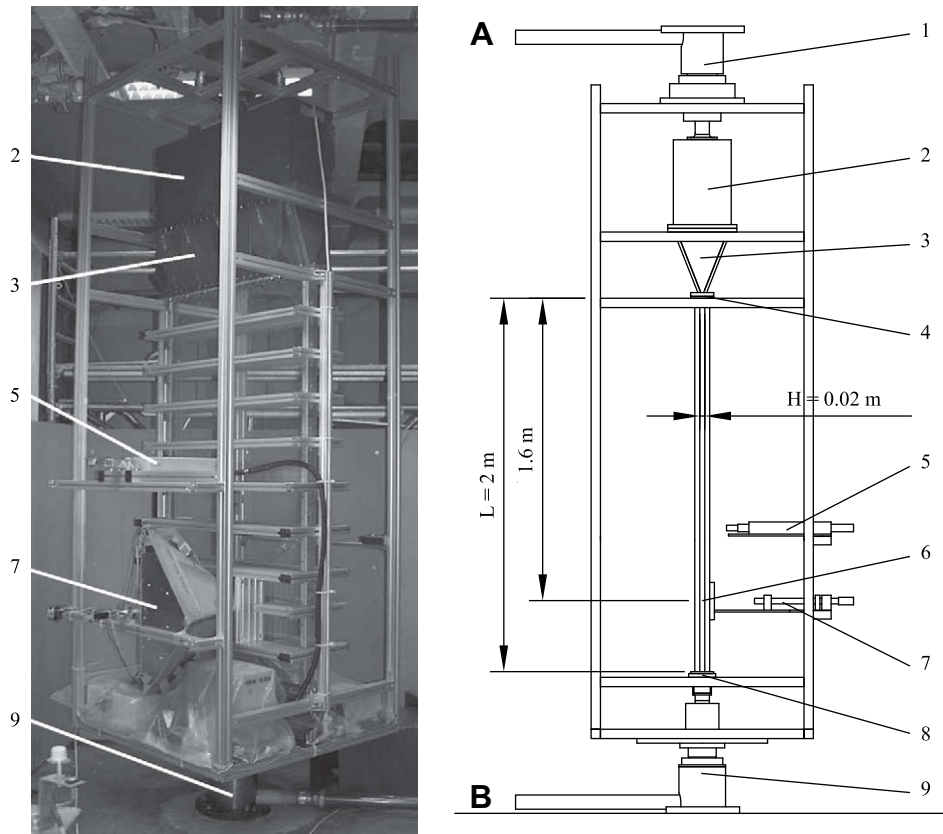
Fig. 1. Setup of the rotating channel section: A: inlet; B: outlet; 1: rotating union; 2: flow straightener; 3: inlet hopper; 4: tripping edge at channel inlet; 5: laser head mount; 6: location of the measuring section; 7: camera mount; 8: channel outlet; 9: rotating union.

The findings are compared with data from the literature, i.e., the results by Kim et al. [9], and with the measurements of the non-rotating channel.

3. Results

An overview of the parameters of the experimental and numerical investigations is given in Table 3. Note, firstly the channel flow at $Re_m = 2850$, i.e., $Re_\tau = 180$, is analyzed. This main part of the discussion is meant to evidence the impact of the rotation speed on the overall flow structure. Secondly, the flow problem at the much smaller Reynolds number $Re_{m,\ l} = 665$ is considered. At this Reynolds number the non-rotating channel flow is laminar. In extending the analysis of the aforementioned $Re_m = 2850$ problem, it is the purpose of this discussion to show that the flow pattern is clearly characterized by the rotation and that the state of the corresponding non-rotating channel flow, be it laminar or turbulent, has negligible impact.

The organization of the $Re_m = 2850$ problem is as follows. First, the properties of the mean flow in the streamwise and the spanwise direction will be discussed to show the influence of the rotation on the time-averaged flow field. Due to the discrepancies between the experimental and numerical data observed in [7] especially in the qualitative behavior an in-depth comparison of the PIV and LES findings is presented. The analysis focuses on the impact of the formulation of the spanwise boundary condition, i.e., no-slip vs. periodic, and the experimental comparison of the spanwise extent of the computational domain.

Having presented the quality of the agreement of the experimental and numerical findings the discussion concentrates on the flow physics which has been initiated in [7]. However, due to the

differences in the numerical and experimental results, a final evaluation could not be given.

Then, the Reynolds stresses will be analyzed to evidence the effect on the fluctuations of the flow. Finally, the two-point correlations will be examined to identify the significance of the rotation
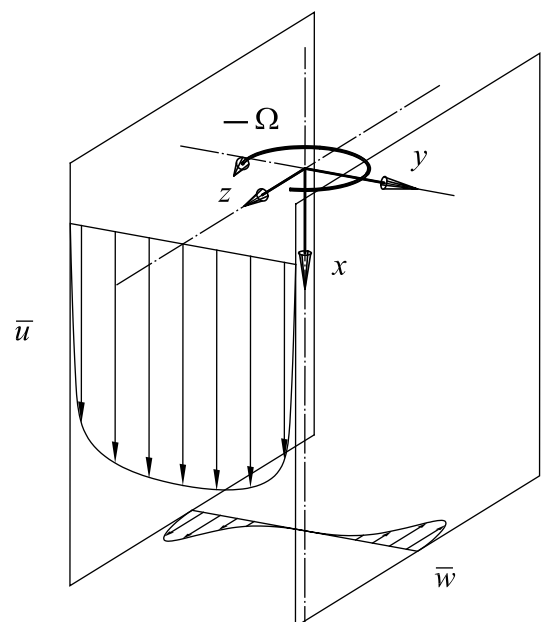

Fig. 2. Coordinate system: x: streamwise direction; y: wall-normal direction; z: spanwise direction; Ω: rotational direction about the streamwise axis.
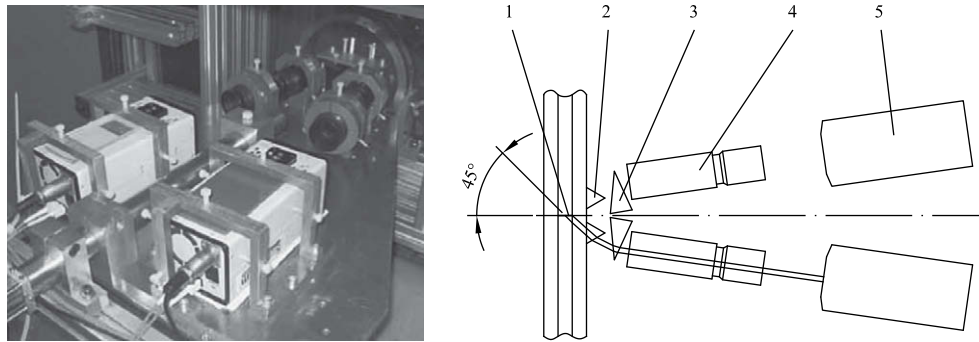
Fig. 3. Setup of the stereoscopic camera system: 1: measuring section; 2: decoupling prism; 3: correction prism; 4: double telecentric lens; 5: CCD double-shutter camera. Two exemplary rays with an observation angle of 45° onto the measuring plane are displayed to illustrate the path of the laser light through the optical setup.

on the size of the coherent structures of the flow. Based on this line of discussion a comprehensive overview on the interaction of the rotation with the mean and the fluctuating properties of turbulent channel flow will be given.

In all figures, the spatial coordinates are normalized by the channel half-height h and the velocities by the mean bulk velocity U. The experimental results are shown on the left-hand side of the figures, while the numerical results appear on the right-hand side. The DNS results of Kim et al. [9] of the non-rotating channel are included in Fig. 5 showing the mean velocity profiles and in Fig. 9 containing the Reynolds stresses as reference values for non-rotating channel flow. Note, the DNS distributions are also shown on the left-hand side.

3.1. Channel flow at $Re_m = 2850$

3.1.1. Mean streamwise flow profile

It has been shown in [7] and [8] that the time-averaged velocity $\overline{u}$ scaled by the mean bulk velocity U decreases along the channel axis and that it develops a steeper velocity gradient near the wall at increasing rotation rate. In other words, the velocity distribution spreads in the wall-normal direction and becomes bulkier at higher rotation rates. This rearrangement of the velocity distribution indicates a stronger momentum exchange due to rotation and as such a change in the friction velocity. The wall-shear stress in the experiments varies since it is the flow rate which is held constant at

the different flow conditions. In the LES [8], on the other hand, the friction velocity based Reynolds number Re_τ or equivalently the pressure gradient is kept constant, which leads to a slightly changing flow rate in the individual computations. Nonetheless, using the experimental and computational mean bulk velocity, respectively, to normalize the data the numerical and experimental results of the mean velocity distributions possess a good agreement.

An enlargement of the core region is shown in Fig. 5 to emphasize the impact of the rotation rate on the mean streamwise flow profile. Due to the rotation the peak values are reduced by 0.032 in the experimental and by 0.022 in the numerical distributions, which correspond to a reduction by 2.7% and 2.2%, respectively. Even though the simulation generates values near the axis which are slightly too small ($\Delta U_{max}/U_{ExP, max} \approx 0.04$), an observation which was also made in the DNS in [7], the qualitative changes in the profile match very well. Moreover, a closer analysis reveals the intersection points of the profiles at different rotation speeds to lie closer together when comparing the PIV results with the LES than with the DNS solutions, i.e., $y/h_{ExP} \approx 0.45$ vs. $y/h_{LES} \approx 0.55$ vs. $y/h_{DNS} \approx 0.65$.

3.1.2. Mean secondary flow profile

The rotation about the main flow axis induces a secondary flow in the plane perpendicular to the rotation axis as is shown in Fig. 6. Near the wall a mean velocity profile in the rotational direction develops depending on the rotation rate. The higher the rotational speed, the larger the peak value of the velocity distribution. Near the channel
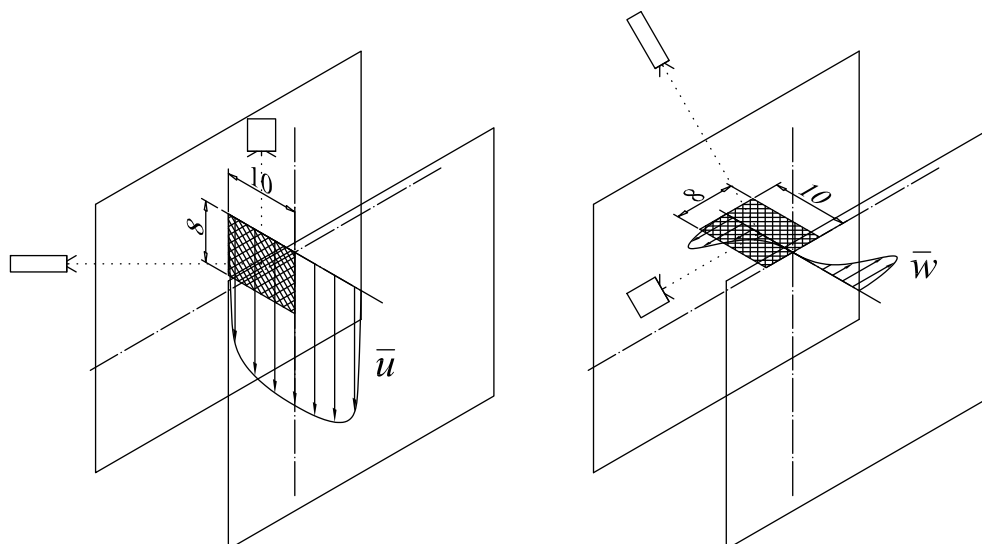

Fig. 4. Light sheet alignment, the values are given in mm. Left: Streamwise orientation to record the main flow component u without deviation. Right: Spanwise orientation to measure the undisturbed secondary flow component w.

Table 1
Parameters of the flow channel.

Channel length	$L = 2$ m
Channel span width	$W = 0.2$ m
Channel height	$H = 0.02$ m
Running length to observation window	1.6 m $\triangleq$ 80% of channel
Ratio running length/wall distance	3.2
Pump output	max. 25,000l/h
Mean bulk flow velocity	$U = 0{-}0.35$ m/s
Rotation rate	$f = 0{-}1.0$ Hz

center the flow structure is less distinct and tends to reverse the flow direction at higher rotation rates and smaller Rossby numbers, respectively. This tendency is somewhat stronger in the numerical than in the experimental distributions. Whereas in the region of the rotation axis, i.e., $-0.5 \leq y/h \leq 0$, a difference in the experimental and numerical data is observed, a convincing agreement is achieved in the near-wall region. Note, the DNS solutions in [7] show an even more pronounced recirculation region near the rotation axis. To shed some light on this discrepancy of the LES and DNS distributions and to substantiate the tendency of only a mild or incipient circulation region being indicated by the LES and the PIV findings a more detailed discussion of the susceptibility of the latter is given.

First, let us recapitulate the results of the analysis of the impact of the spanwise extension on the flow field near the rotation axis. The findings at three span widths, $W = 0.2$ m, $W = 0.5$ m, and $W = 1.0$ m for the highest rotation rate shown in Fig. 7 confirm that the spanwise extent of the channel does not influence the qualitative distribution of neither $\bar{u}$ nor $\bar{w}$. The only difference in the $\bar{w}$-profiles is a slightly larger value of the $\bar{w}$-velocity near the wall at larger span width, while the shape of the profile remains unchanged. Especially the measurements of the flow structure near the axis show no variation whatsoever. In other words, the assumption that the flow field determined in the experiments is influenced by the finite span width of the channel is refuted if W is larger than $W = 0.2$ m.

Next, the influence of the formulation of the spanwise boundary condition on the reverse flow region was investigated. That is, various large-eddy simulations were performed. First, the full channel setup was simulated by prescribing no-slip conditions on the spanwise boundaries. Second, periodic boundary conditions were imposed in the spanwise direction such that only the aforementioned spanwise extent of 20 h was captured. The findings of the mean secondary distribution $\bar{w}/U$ at $Ro_m = 65.2$ are shown in Fig. 8. Although the numerical profiles almost match it is fair to conclude that the recirculation region near the rotating axis is somewhat smaller, when the no-slip boundary condition is imposed, than the reverse flow region at periodic boundary conditions. Note, the former solution, i.e., the smaller recirculation near the channel center, is in close agreement with the experimental findings. This investigation shows that even at a spanwise

Table 2
Parameters of the PIV-system.

Cameras	PCO SensiCam Doubleshutter
Resolution	1280×1024 pixel
Sampling rate	3 Hz
Lenses	Sill S5PJ7031 double telecentric lenses
Laser	Continuum® MiniLite Nd:YAG
Observation area size	8 mm $\times$ 10 mm
Light sheet thickness	≈ 0.2 mm
Average particle size	20 µm
Correlation window size	32×32 pixel
Correlation window overlap	50%
Spatial resolution	0.35 mm $\times$ 0.3 mm
Approx. Δx^+ and Δz^+	≈ 5.4
Approx. Δy^+	≈ 6.3

Table 3
Parameters of the PIV and LES investigations.

PIV		LES	
$Re_m = 2850$ ($\triangleq Re_\tau = 180$)			
$f = 0$ Hz	$Ro_m = \infty$	$f = 0$ Hz	$Ro_m = \infty$
$f = 0.46$ Hz	$Ro_m = 65.2$	$f = 0.46$ Hz	$Ro_m = 65.2$
$f = 0.75$ Hz	$Ro_m = 40$	$f = 0.8$ Hz	$Ro_m = 37.5$
$Re_{m,\,l} = 665$			
$f = 0$ Hz	$Ro_{m,\,l} = \infty$		
$f = 0.46$ Hz	$Ro_{m,\,l} = 15.2$		
$f = 0.75$ Hz	$Ro_{m,\,l} = 9.3$		
$f = 1.0$ Hz	$Ro_{m,\,l} = 7.0$		
Variations			
Boundary conditions of the LES at $Ro_m = 65.2$			
No-slip		Periodic	
Span width of PIV measurements at $Ro_m = 40$			
$W = 0.2$ m	$W = 0.5$ m	$W = 1.0$ m	

extent of the computational domain of 20 h the boundary conditions do have a slight impact on the quantitative distributions of the mean secondary profile $\bar{w}$. This impact is even more pronounced when periodicity is enforced on a smaller span width as has been done in earlier DNS investigations in [5,6,14], which all resulted in a distinct S-shape over the channel half-height. In those computations the extension of the spanwise periodicity of the computational domain was based on that of the non-rotating channel flow, i.e., it was defined as $2\pi h \approx 6.2\ h$ and as such it was much smaller than in the present study where the span width was 20 h. Therefore, the reasonable agreement between the current LES and PIV findings as far as the magnitude of the secondary flow is concerned shows the assumption of too small a spanwise periodicity to generate too strong a recirculation near the rotation axis.

Nevertheless, it is also evident in Fig. 8 that the marginal reverse flow detected in the LES data was not resolved in the experiments. The reason for this structure to be not detected in the experimental results appears to be, that this pattern is very susceptible to small external disturbances such as vibrations or irregularities of the channel walls. In other words, the generation of the reverse flow is so sensitive that it is suppressed by the current setup of the rotating channel measurement facility. If it were simply an issue of the
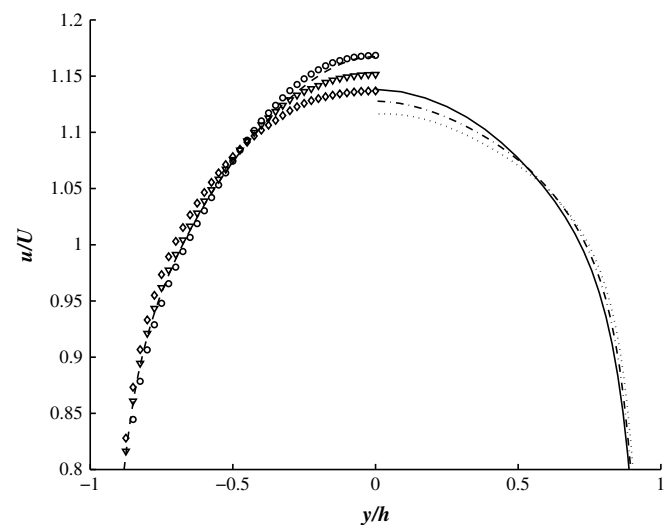

Fig. 5. Core region of the mean velocity profiles $\bar{u}/U$. DNS of non-rotating case by (9) - - -; Experiment: $Ro_m = \infty$ ○, $Ro_m = 65.2$ ▽, $Ro_m = 40$ ◇; LES: $Ro_m = \infty$ —, $Ro_m = 65.2$ -⋅-⋅-, $Ro_m = 37.5$ ⋯.

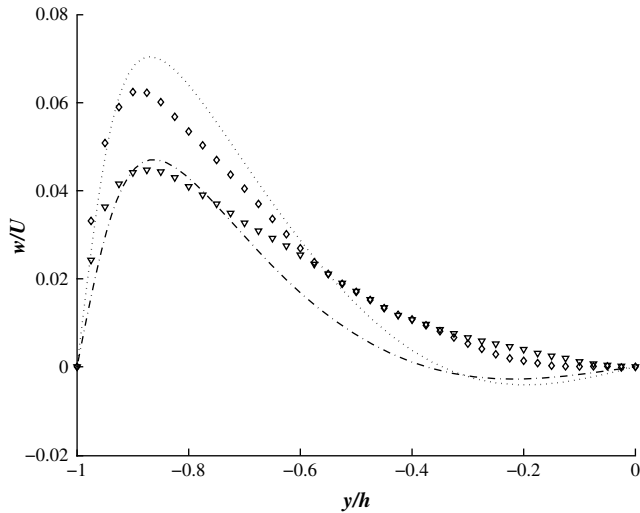**Fig. 6.** Mean secondary profiles $\overline{w}/U$. Experiment: $Ro_m = 65.2$ ▽, $Ro_m = 40$ ◇; LES: $Ro_m = 65.2$ ‑‑‑‑, $Ro_m = 37.5$ ….

measuring accuracy decreasing towards the channel axis, the effect would be visible in the remaining well resolved profile. That is, the gradient of the velocity distribution in the region between $-0.8 \leq y/h \leq -0.2$ would be similar to that of the LES.

Since the mean secondary flow points in the circumferential direction, the larger velocities near the wall are directly related to the Coriolis effect. The main contribution comes from the wall-normal velocity fluctuations, while the main flow component obviously has no effect being parallel to the rotation axis. The small mismatch in the distributions in Fig. 6 at the highest rotation rate near the wall, i.e., at $Ro_m = 37.5$ in the computation and $Ro_m = 40$ in the experiment, can be attributed to the slightly smaller mean Rossby number, i.e., higher rotation rate, used in the numerical simulation.

3.1.3. Reynolds stresses

In Fig. 9 the Reynolds stresses of the streamwise and spanwise components are shown since they can be measured directly with one of the two light sheet orientations. The distributions show the increase of the Reynolds stresses and the satisfactory agreement of the experimental and numerical data especially for the streamwise component.

The distributions of the experimental spanwise fluctuations w' are slightly less conclusive since the values of the non-rotating case are higher than those of the rotating channel. This seems to be due to sensitivities of the measurement. Since the spanwise velocity component is much smaller than the streamwise component, it is susceptible to even minimal deviations of the camera alignment. Therefore, it is more appropriate to focus on the rotating results. The tendency of increased turbulence is evident in the two rotating flows. This increase is also observed at a lower Rossby number of $Ro_m = 30$ the distribution of which is not displayed in Fig. 9. Furthermore, the investigations at varying channel spans showed beginning from a low distribution in the non-rotating case a similar increase in the overall distributions of the spanwise fluctuations.

The most obvious change is visible in the shear stresses containing the spanwise fluctuation w', i.e., they become non-zero under rotation, as displayed in the bottom image of Fig. 9. The distributions grow significantly in a rotating system especially in the near-wall region. That is, they evidence the pronounced impact of the rotation on the near-wall flow which is already indicated in the distributions of the normal Reynolds stresses. Exemplarily, the $\overline{u'w'}$ distributions are given in Fig. 9. Although the numerical and experimental data do not match quantitatively, the strong dependence of the Reynolds shear stress distribution on the rotation speed is analogously captured in both investigations.

In brief, turbulence is augmented in all coordinate directions by the rotation, while the main flow component experiences the least increase. The tendency of the fluctuations to increase stronger in the core flow, which is evident in the LES data, is also noticeable in the measurements. Even though there are some quantitative differences, the qualitative changes due to the rotation are similar in the experiments and simulations.

Note, the LES results match the experimental data better than the DNS results from [7]. The PIV and LES based streamwise Reynolds stress distributions possess an increase in the values on the centerline of approximately 20% in the experiment and 10% in the simulation. Their overall shape is not changed at all. The DNS solutions from [7], however, show a stronger growth of about 50% of the values near the channel axis, while the values near the wall grow only slightly. A similar conspicuity appears in the spanwise Reynolds stress distributions. The overall increase of the values is apparent in all three data sets. However, the DNS data show, unlike the LES and the PIV distributions, an overly large growth near the channel axis, such that a local minimum occurs near $y/h = \pm 0.35$ and a maximum exists on the channel centerline.

3.1.4. Two-point correlations

To further analyze the turbulent flow field the two-point correlations are considered. The two-point velocity correlation tensor is defined by
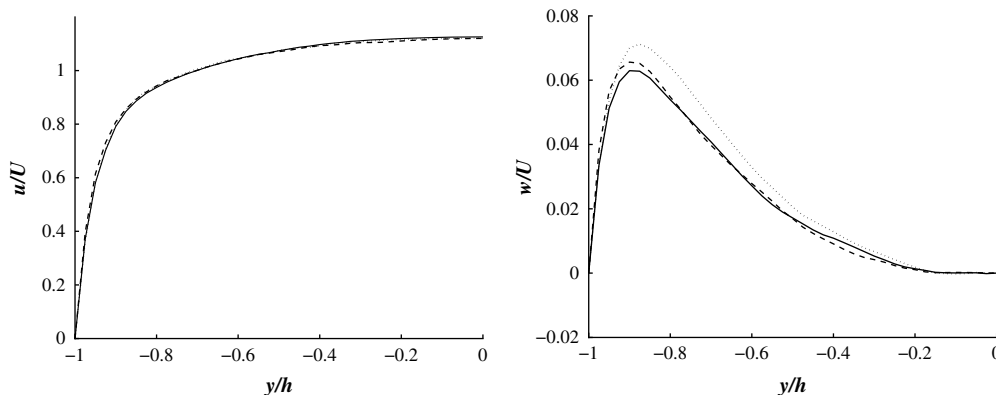

Fig. 7. Comparison of the mean velocity profiles $\overline{u}/U$ and $\overline{w}/U$ at different channel span widths W for $Ro_m = 40$. $W = 1.0$ m …, $W = 0.5$ m - - -, $W = 0.2$ m —.
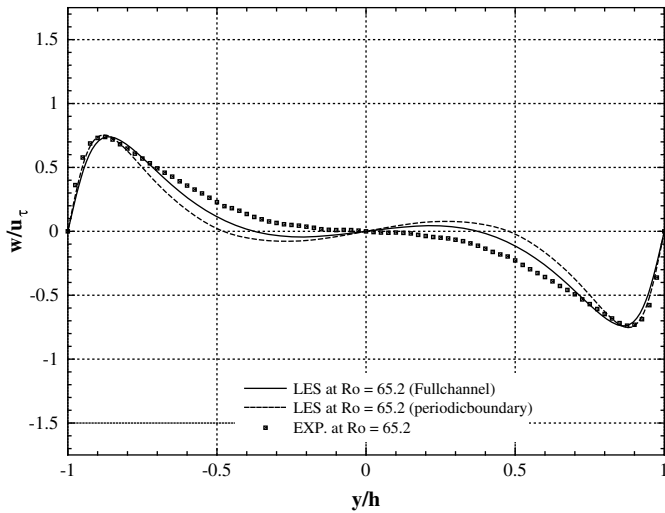
Fig. 8. Comparison of the influence of different computational boundary conditions on the mean secondary velocity profile $\overline{w}/u_\tau$ at $Ro_m = 65.2$ and the experimental result.

$$R_{\alpha\beta}(r) = \frac{\overline{u'_\alpha(x,t)u'_\beta(x+r,t+\tau)}}{\sqrt{\overline{u'^2_\alpha(x,t)}}\sqrt{\overline{u'^2_\beta(x+r,t+\tau)}}}, \qquad (2)$$

where u'_α and u'_β are the fluctuating velocity components in a Cartesian coordinate system α, $\beta = 1$, 2, 3, r is the distance between the two points in the frame of reference, and τ is the time delay of the signal of u'_β. From this space–time correlation we will

consider the space correlation functions only, i.e., $\tau = 0$, and as such the coherence of the signal at two different coordinate positions in the same instant is determined. The two-point correlations are investigated to evidence the coherence of the flow structures and as such to get an impression of the variation of the turbulent length scales under rotation.

However, it is emphasized that the results of the experiments can be considered only qualitative findings. It is the tendency that is to be evidenced and not the quantity that will be analyzed in the discussion.

In Fig. 10 PIV and LES based R_{uu} and R_{ww} distributions in the streamwise direction are juxtaposed. The base point is located at $y/h = 0.3$ off the wall. In Fig. 11 the correlations at $y/h = 0.3$ in the spanwise direction are displayed. Finally, Fig. 12 shows R_{uu} and R_{ww} in the spanwise direction at a base point $y/h = 0.12$. That is, these latter correlations evidence the structures in the area of the maximum secondary velocity and u-RMS values.

The measuring section in the experiment only covers 8 mm × 10 mm, while the simulation yields values over a range of 200 mm in the streamwise and spanwise directions. In Figs. 10–12 the development of the correlation functions is presented over a range of $x/h = 2$ and $z/h = 2$, respectively, which is larger than the range of the experimental data. However, this presentation allows an immediate comparison of the distributions close to the respective base point. Note, the distributions shown in these figures do not cover the entire computational domain which is why the correlations do not asymptotically vanish.

Figs. 10 and 11 evidence the streamwise and spanwise correlations to rise at increasing rotation rate. In other words, the coherent structures become longer and wider and the length scales of the flow grow. Closer to the wall, i.e., at $y/h = 0.12$, this behavior is
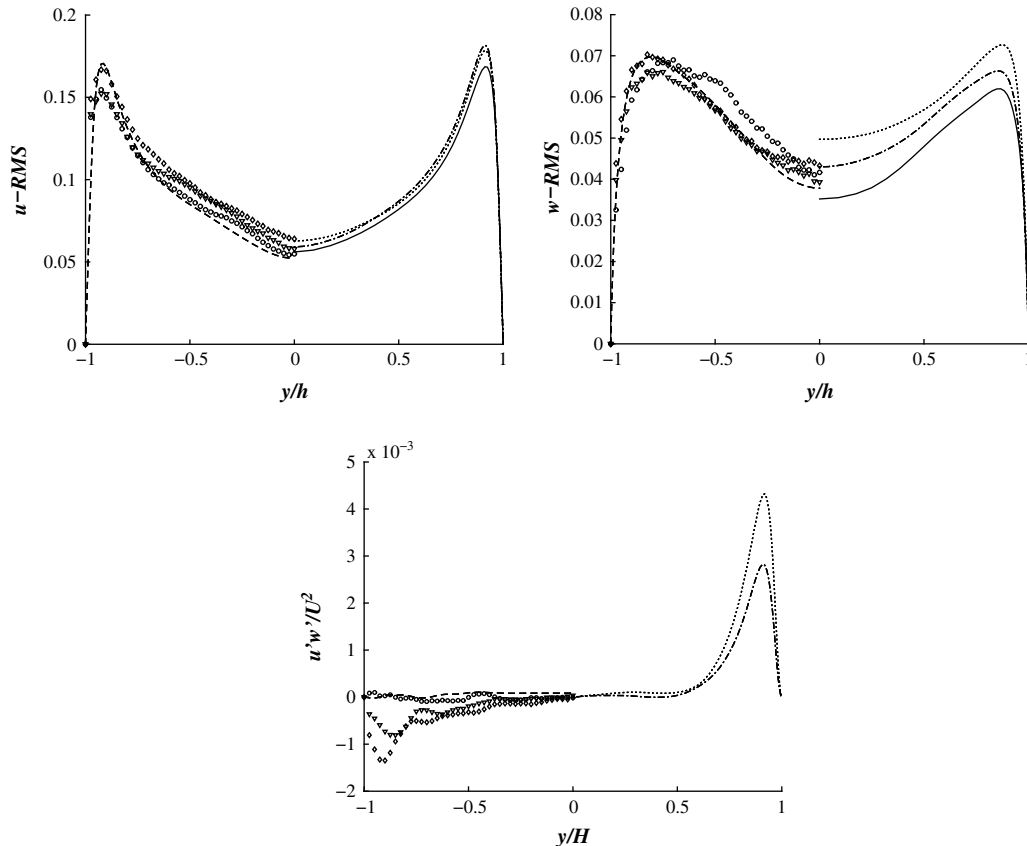

Fig. 9. Reynolds stresses $\sqrt{\overline{u'^2}}/U$, $\sqrt{\overline{w'^2}}/U$ and $\overline{u'w'}/U^2$. Left: DNS of the non-rotating case by [9] - - -, Experiment: non-rotating case $Ro_m = \infty$ ○, $Ro_m = 65.2$ ▽, $Ro_m = 40$ ◇; Right: LES: $Ro_m = \infty$ —, $Ro_m = 65.2$ ·-·-·, $Ro_m = 37.5$ ·····.
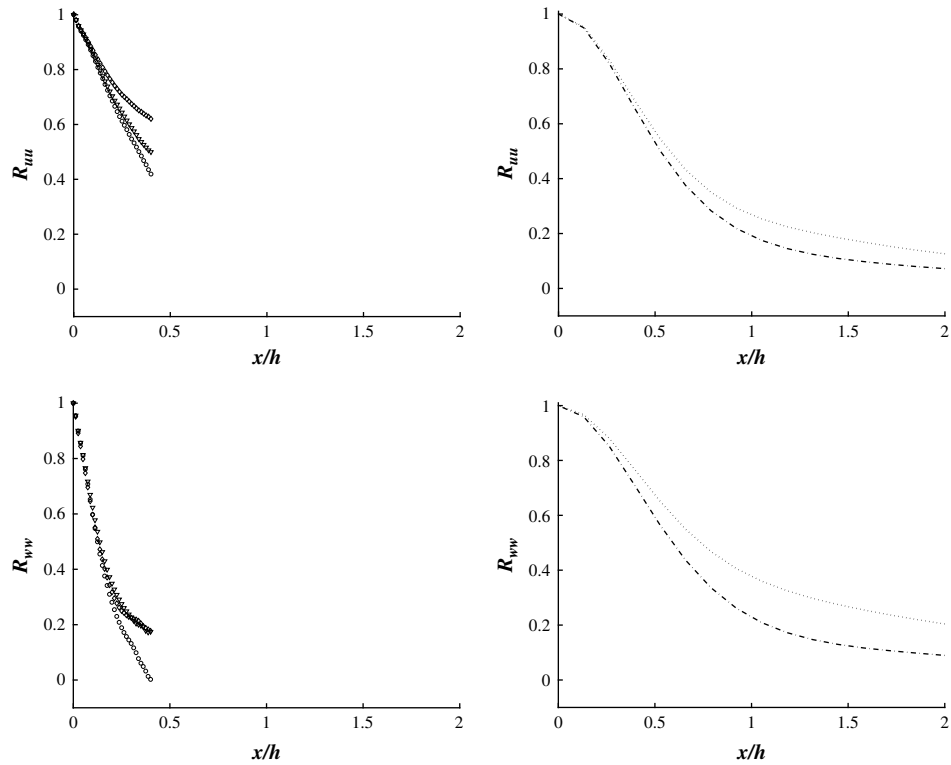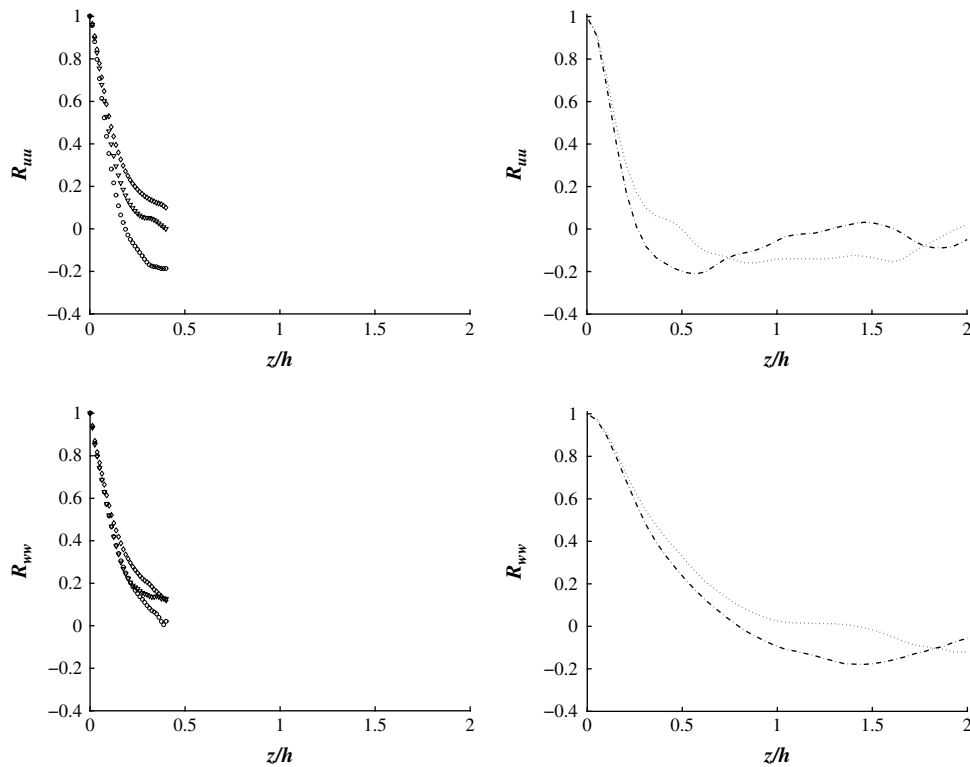
Fig. 10. Two-point correlations in the streamwise direction at $y/h = 0.3$, measured from the wall. Left: PIV, top: R_{uu}, bottom: R_{ww}; non-rotating case $Ro_m = \infty$ ○, $Ro_m = 65.2$ ▽, $Ro_m = 40$ ◇. Right: LES, top: R_{uu}, bottom: R_{ww}; $Ro_m = 65.2$ -⋅⋅⋅-, $Ro_m = 37.5$ ….

Fig. 11. Two-point correlations in the spanwise direction at $y/h = 0.3$, measured from the wall. Left: PIV, top: R_{uu}, bottom: R_{ww}; non-rotating case $Ro_m = \infty$ ○, $Ro_m = 65.2$ ▽, $Ro_m = 40$ ◇. Right: LES, top: R_{uu}, bottom: R_{ww}; $Ro_m = 65.2$ -⋅⋅⋅-, $Ro_m = 37.5$ ….
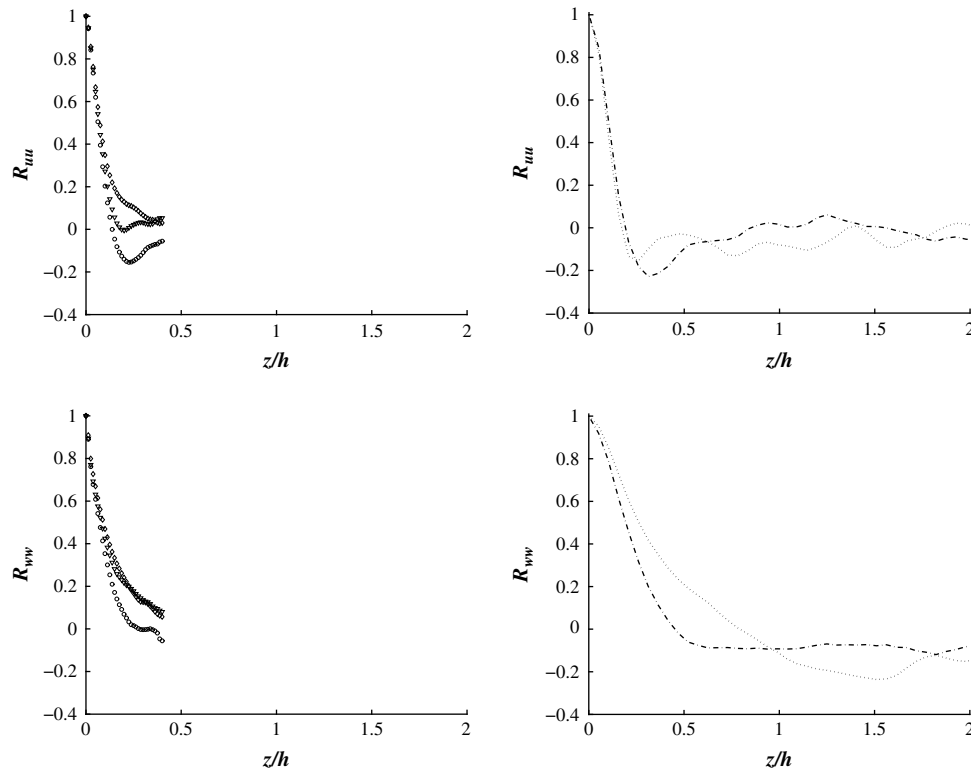
Fig. 12. Two-point correlations in the spanwise direction at $y/h = 0.12$, measured from the wall. Left: PIV, top: R_{uu}, bottom: R_{ww}; non-rotating case $Ro_m = \infty$ ○, $Ro_m = 65.2$ ▽, $Ro_m = 40$ ◇. Right: LES, top: R_{uu}, bottom: R_{ww}; $Ro_m = 65.2$ -··-, $Ro_m = 37.5$ ….

slightly different. While the correlation of the spanwise velocity component weakly grows in the immediate vicinity of the wall, the correlation of the streamwise component hardly changes.

Overall, the results indicate a general growth of the coherent structures outside the immediate vicinity of the wall, i.e., at $y/h \geq 0.3$. In the near-wall region, i.e., in the region of the highest shear, however, the growth of the spanwise correlations is limited to the spanwise velocity component, while the streamwise length scale remains more or less the same. Even though the quantitative findings do not match exactly, the tendency and even the general shape are alike in the experiment and the simulation.

Note, the length scales of the correlations differ between the PIV data and the LES solutions. It must be stated that it is practically impossible to determine any reliable length scale from the experimental results, since the observation area is far too small to retrieve a sufficient section of the correlation distribution. Thus, no sound quantitative difference can be discussed based on the length scale.

The experimental results appear to be smaller than the numerical findings. A similar difference is also visible in the comparison between PIV and DNS data in [7]. This deviation could be caused by the varying number of samples in the experimental and numerical analysis. The experimental data are based on 750 images instead of 2800 in the numerical simulation. It can be conjectured that this number of experimental samples is too small to reach the same degree of correlation that is found in the results of the numerical simulations. This is supported by the observation that when the number of data in the numerical findings have been reduced the numerical distribution showed a tendency to shift towards the experimental findings. This suggests that, while the experimental data are evidently sufficient to resolve the mean and the transient properties of the flow, the higher-order moments require a larger amount of samples to acquire a similar quality. This conjecture is supported by the distributions of the two-point correlations in [15] which are based on 4410 samples.

Furthermore, in LES computations the subgrid scales are modelled, that is, other than in a DNS, where all the scales down to the Kolmogorov scales are resolved, a filtered velocity field is determined. This filtering influences the two-point correlations such that the length scales are computed larger than they are in a non-filtered solution. Therefore, a deviation between numerics and experiment occurs. However, it has to be emphasized that while the values do not match exactly, the reaction of the correlations to rotation, i.e., an increase of the length scales, is the same in the experimental and the numerical analyses.

3.1.5. Coherent structures

Coherent structures are relatively strong quasi-streamwise vortices which stretch along the streamwise direction. They occur in counter-rotating pairs and in chains of overlapping vortices in the streamwise direction. They interact with each other, are lifted from the wall, and increase with the distance from the wall due to self-induction. Off the wall, they begin to oscillate and finally, lead to a rapid breakdown with an increase in small-scale, chaotic motion. This phenomenon of coherent structure breakdown is called burst. Following a burst, high-speed fluid moves towards the wall to sweep away the fluid from the former burst event. This transport of high-speed momentum increases the friction drag on the wall.

To illustrate the impact of the rotation rate on the shape and size of the coherent structure, an instantaneous visualization of the near-wall coherent structures based on the LES data for the non-rotating turbulent channel flow at $Ro_m = \infty$ and the rotating cases at $Ro_m = 65.2$ and $Ro_m = 37.5$ is given by λ_2-contours [16] in Fig. 13. In the non-rotating case only small and disordered structures are visible, while coherent structures drastically increase at growing Rossby number. It is observed that at increasing rotation speed longer and also thicker coherent structures in the streamwise direction appear. Compared with the λ_2-contours of the non-rotating case, the turbulence intensity is enhanced especially in the
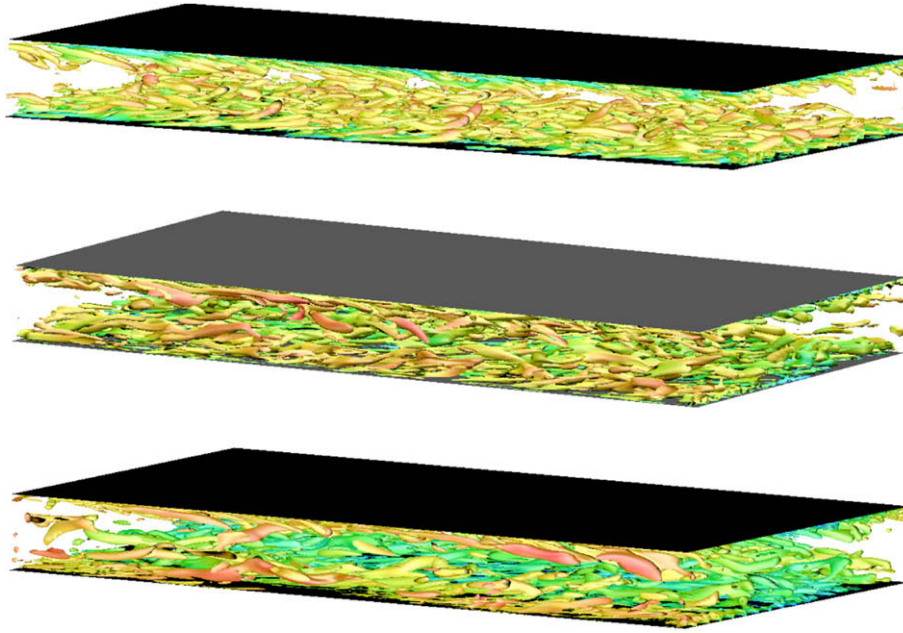
Fig. 13. Coherent structures within the flow, identified by the λ_2-criterion. Top: non-rotating channel; center: $Ro_m = 65.2$; bottom: $Ro_m = 37.5$.

center plane when the rotation speed is increased. The comparison of these figures clearly demonstrates the higher rotation speed to lead to larger coherent structures distributed over almost the entire channel, as has already been indicated by the analysis of the correlation functions.

3.2. Channel flow at $Re_{m, l} = 665$

As has been mentioned before, a lower flow rate was investigated to see the impact of rotation on laminar base flow. In this measurement campaign the mean bulk velocity was reduced to 0.07 m/s, leading to a bulk Reynolds number of $Re_{m, l} = 665$. In these measurements the tripping edge was removed from the channel inlet, i.e., the entering flow is not artificially perturbed. The same rotation frequencies and one higher frequency as in the turbulent case were chosen, i.e., $f = 0.0$ Hz, $f = 0.46$ Hz, $f = 0.75$ Hz, and $f = 1.0$ Hz. This results in Rossby numbers $Ro_{m, l} = \infty$, $Ro_{m, l} = 15.2$, $Ro_{m, l} = 9.3$, and $Ro_{m, l} = 7.0$. It is evidenced in Fig. 14 that the non-rotating channel possesses a laminar profile. At the smallest rotation frequency $f = 0.46$ Hz, i.e., $Ro_{m, l} = 15.2$, the velocity distribution takes on a typical turbulent shape. Once transition has occurred this velocity profile is rather independent from the rotation rate. Obviously, the small disturbances which are damped in laminar flow

under non-rotating conditions are augmented severely by the rotation and cause the flow to become turbulent.

In rotating turbulent pipe flow an increase of the rotation rate shows a tendency of the profile to approach a parabolic shape similar to the distribution in laminar flow [17]. In other words, the rotation stabilizes the flow and a laminar velocity distribution is observed even at higher Reynolds numbers. At rotating pipe flow the circumferential velocity is increased such that there is only an indirect impact via the continuity equation on the radial and the streamwise velocity components, which define the dominant turbulence production term. In the experiment of the channel rotating about the streamwise axis which has been discussed above the initial flow is laminar instead of turbulent as in [17]. Due to the increasing rotation the normal velocity component is directly influenced by the channel movement. Furthermore, disturbances in the wall-normal velocity component are linked to the spanwise velocity component via the continuity equation. The growth of these spanwise fluctuations, which is shown in Fig. 15, substantiates this hypothesis. This destabilization is very much in line with recent results concerning rotating laminar pipe flows. It has been shown by DNS in [18] that laminar pipe flow is destabilized and becomes turbulent under axial rotation. Thus, these results confirm the observations of the current laminar channel flow development.
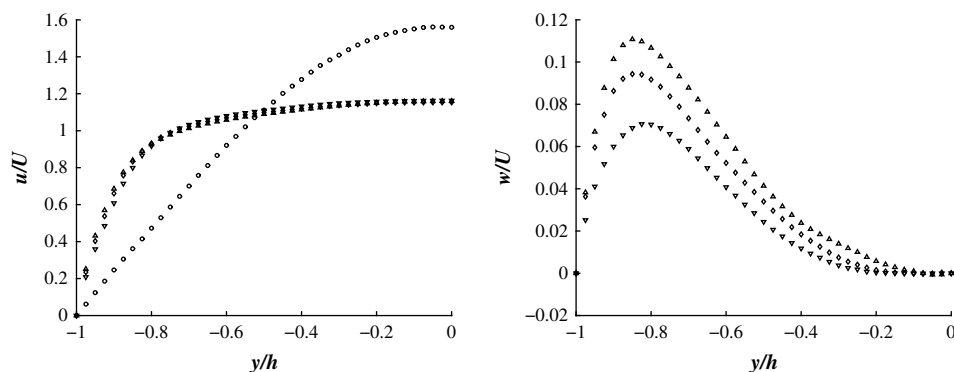

Fig. 14. Comparison of the mean main flow $\bar{u}/U$ (left) and the mean secondary flow $\bar{w}/U$ (right) at $Re_{m, l} = 665$. Non-rotating case $\circ$, $Ro_{m, l} = 15.2$ $\triangledown$, $Ro_{m, l} = 9.3$ $\diamond$, $Ro_{m, l} = 7.0$ $\triangle$.
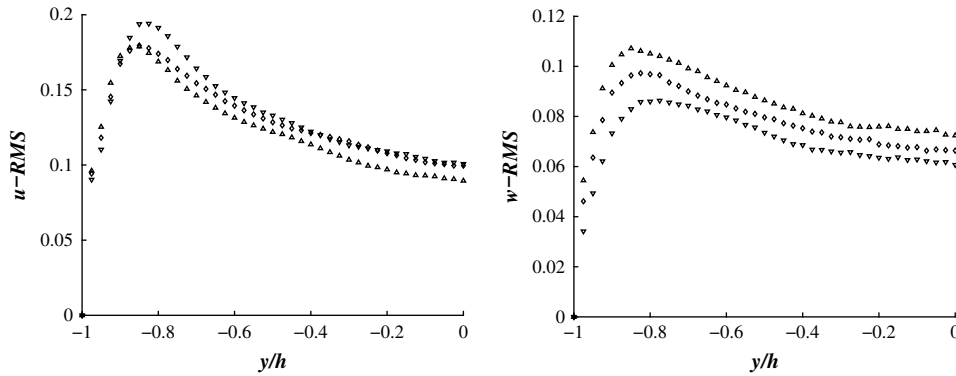
Fig. 15. Comparison of the RMS values of the flow at $Re_{m,l} = 665$ for $\sqrt{\overline{u'^2}}/U$ (left) and $\sqrt{\overline{w'^2}}/U$ (right). $Ro_{m,l} = 15.2\ \triangledown$, $Ro_{m,l} = 9.3\ \diamond$, $Ro_{m,l} = 7.0\ \triangle$.

The increase of the normal velocity component through the modified boundary condition strongly enhances the momentum exchange in the normal direction even at low Reynolds numbers such that a turbulent flow field develops in a rotating channel in a Reynolds number range in which the flow in a non-rotating channel still is laminar.

Due to the rotation-induced turbulence, the flow develops the same secondary profile already known from the high Reynolds number measurements. The shape of the profile is more or less the same, i.e., the secondary motion develops a maximum near the wall and vanishes in the area of the rotation axis. A visible reverse flow does not appear although the number of revolutions, which the flow undergoes before it reaches the measuring section, is quadrupled compared to the high Reynolds number case. Thus, the revolution history of the flow does not seem to have a significant impact on the distribution of the secondary flow, at least not on the development of a reverse flow. However, it has to be kept in mind that the flow in this case is originally laminar and thus might develop differently.

The turbulent character of the low Reynolds number flow under rotation is also evident in the distributions of the Reynolds stresses in Fig. 15. Clearly, the shape of the profiles is similar to that of the high Reynolds number findings. The apparent decrease of the values in the $\sqrt{\overline{u'^2}}/U$ profiles is due to a slight increase of U at increasing rotation rate. The comparison of the non-normalized RMS values shows that $\sqrt{\overline{u'^2}}$ hardly depends on the rotation speed. This outcome more or less matches the findings in the high Reynolds number flow, where the fluctuations of the main flow component experience the least change. The normalized and non-normalized RMS values of the w-component show the same evident increase as the high Reynolds number flow under rotation.

To evidence the impact of the rotation speed on the mean velocity distribution, measurements were performed at an increasing rotation rate, starting at no rotation and constantly increasing the rotation up to $f = 1.0$ Hz. The comparison of the instantaneous velocity profiles in Fig. 16 shows, the distribution to clearly deviate from a parabola at a Rossby number larger than $Ro_m = 35$. A closer analysis of the individual images taken during the measurement indicates turbulent flow at $Ro_m \approx 50$. In this case transition is defined by the decrease of the centerline velocity by more than 20% and the simultaneous increase of the velocity at $y/h = 0.2$ by more than 50%.

4. Summary

PIV and LES findings of a turbulent channel flow rotating about the streamwise axis at several Rossby numbers have been discussed and compared. The results show a convincing qualitative and quantitative agreement of the mean velocity properties and the tendencies in the development of the fluctuation properties to be very similar. In both investigations growing rotation rates lead to increasing flow rate near the wall region and thus a fuller velocity profile. Additionally, the LES results have been shown to quantitatively agree much better with the measurements than earlier DNS data regarding the changes in the mean profile as well as especially the secondary flow associated with the Coriolis force.

The comparison of computations based on no-slip and periodic boundary conditions in the spanwise direction shows the simulation of the walls to have some influence on the size of the reverse flow region. Experiments at different channel widths show hardly an impact on the secondary velocity profile besides a minor effect on the quantitative distribution. The normal stresses of the flow barely grow in the streamwise direction, while they clearly increase in the spanwise direction. The shear stresses containing the spanwise velocity change dramatically, i.e., they strongly increase at higher rotation rates.

In brief, the LES data discussed in this article agree better with the PIV results than previous DNS results. In fact, this former DNS–PIV discrepancy caused this subsequent analysis. A possible explanation for the mismatch of the DNS results is the prescription of periodic boundary conditions on too small a computational domain in the spanwise direction.
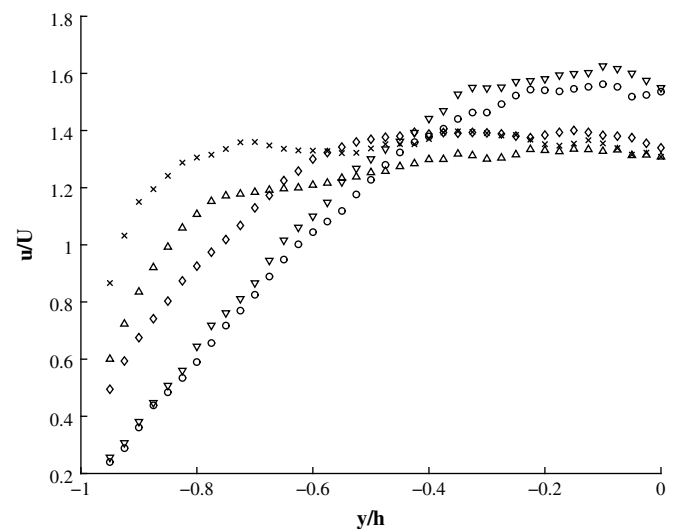

Fig. 16. Instantaneous velocity profiles at $Re_{m,l} = 665$ to illustrate the transition of the flow due to rotation. $Ro_{m,l} = \infty\ \circ$, $Ro_{m,l} = 70\ \triangledown$, $Ro_{m,l} = 35\ \diamond$, $Ro_{m,l} = 23.3\ \triangle$, $Ro_{m,l} = 17.5\ \times$.

PIV measurements at $Re_{m,\,l} = 665$ subject to the same rotation rates as in the $Re_m = 2850$ flow show the flow to become turbulent and to develop a structure analogous to the flow at $Re_m = 2850$. The mean velocity profiles and the Reynolds stress distributions are similar to those at higher Reynolds number, i.e., the velocity gradient strongly increases near the wall and a secondary profile develops in the spanwise direction.

Acknowledgments

References

[1] J.E. Hart, Instability and secondary motion in rotating channel flow, J. Fluid Mech. 45 (1971) 341.

[2] J.P. Johnston, R.M. Halleen, D.K. Lezius, Effects of spanwise rotation on the structure of two-dimensional fully developed turbulent channel flow, J. Fluid Mech. 56 (1972) 533.

[3] R. Kristoffersen, H.I. Andersson, Direct simulations of low-Reynolds number turbulent flow in a rotating channel, J. Fluid Mech. 256 (1993) 163.

[4] D.K. Tafti, S.P. Vanka, A numerical study of the effects of spanwise rotation on turbulent channel flow, Phys. Fluids A 3 (1991) 642.

[5] M. Oberlack, W. Cabot, B.A. Petterson Reif, T. Weller, Group analysis, direct numerical simulation and modelling of turbulent channel flow with streamwise rotation, J. Fluid Mech. 562 (2006) 383.

[6] H. Wu, N. Kasagi, Effects of arbitrary directional system rotation on turbulent channel flow, Phys. Fluids 16 (2004) 979.

[7] I. Recktenwald, T. Weller, W. Schröder, M. Oberlack, Comparison of direct numerical simulations and particle-image velocimetry data of turbulent channel flow rotating about the streamwise axis, Phys. Fluids 19 (2007) 085114.

[8] N. Alkishriwi, M. Meinke, W. Schröder, Large-eddy simulation of rotating turbulent channel flow, Comp. Fluids 37 (7) (2008) 786.

[9] J. Kim, P. Moin, R. Moser, Turbulence statistics in fully developed channel flow at low Reynolds number, J. Fluid Mech. 177 (1987) 133.

[10] R. Konrath, W. Schröder, Telecentric lenses for imaging in particle image velocimetry – a new stereoscopic approach, Exp. Fluids 33 (2002) 703.

[11] M. Meinke, W. Schröder, E. Krause, T. Rister, A comparison of second- and sixth-order methods for large-eddy simulations, Comp. Fluids 31 (4–7) (2002) 695.

[12] F. Rütten, W. Schröder, M. Meinke, LES of low frequency oscillations of the Dean vortices in turbulent pipe bend flows, Phys. Fluids 17 (2) (2005) 035107.

[13] N. Alkishriwi, M. Meinke, W. Schröder, A large-eddy simulation method for low Mach number flows using preconditioning and multigrid, Comp. Fluids 35 (10) (2006) 1126.

[14] O.A. El-Samni, N. Kasagi, The effect of system rotation with three orthogonal rotating axes on turbulent flow, in: Proceedings of ICFDP7, Sharm El-sheik, Egypt (2001).

[15] C.J. Kähler, Investigation of the spatio-temporal flow structure in the buffer region of a turbulent boundary layer by means of multiplane stereo PIV, Exp. Fluids 36 (2004) 114.

[16] J. Jeong, F. Hussain, On the identification of a vortex, J. Fluid Mech. 285 (1995) 69.

[17] P. Orlandi, M. Fatica, Direct simulations of turbulent flow in a pipe rotating about its axis, J. Fluid Mech. 343 (1997) 43.

[18] B.P.M. van Esch, J.G.M. Kuerten, Direct numerical simulation of the motion of particles in rotating pipe flow, J. Turb. 9 (4) (2008) 1.